A Guide to Performing Automatic 2D Near-Field Planar Measurements Using an Outdated Robotic Arm

Alan Fernando Ney Boss^{1,*} (b), Eduardo Alan de Andrade Cruz¹ (b), Alexandre dos Santos Andrade¹ (b), Guilherme Nader Kawassaki¹ (b), Mirabel Cerqueira Rezende² (b), Mauricio Ribeiro Baldan³ (b)

- 1. Instituto Nacional de Pesquisas Espaciais 🕸 Laboratório de Integração e Teste São José dos Campos/SP Brazil.
- 2. Universidade Federal de São Paulo no Laboratório de Tecnologia de Polímeros e Biopolímeros São José dos Campos/SP Brazil.
- 3. Instituto Nacional de Pesquisas Espaciais 🕸 Coordenação de Pesquisa Aplicada e Desenvolvimento Tecnológico São José dos Campos/SP Brazil.
- *Correspondence author: alan.boss@inpe.br

ABSTRACT

Near-field (NF) measurements are commonly used to predict the far-field (FF) of an antenna through NF to FF conversion. Conventional automated setup measurements use linear robotic systems that occupy a large space and are limited to scan multiple planes and co- and cross-polar in a sequence. Modern systems use a robotic arm to overcome this issue, but it is very expensive. This work explains how to perform 2D NF measurements using an outdated robotic arm controlled by Python and Arduino. This low-cost system was validated through horn lens measurements from X- to K_a -band. The maximum difference in beam waist between theoretical and measured was ~3.17 mm for the X-band horn lens antenna due to the focal distance difference of ~11.11 mm. The source of errors and limitations is discussed here. The measured data along with the Python code to generate 2D color maps are available on GitHub. Although it involves more complexity and additional steps compared to commercial systems, this budget system provided good agreement with the theoretical values of the horn lens antennas, becoming a viable alternative to perform raster NF measurements over a three-dimensional volume. Further works may include implementations of cylindrical or spherical measurements.

Keywords: Antenna; Lens; Python; Automation.

INTRODUCTION

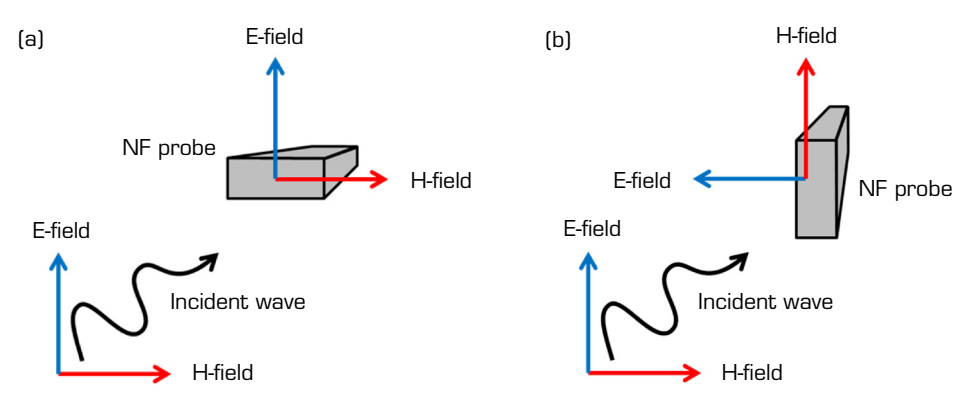
The electromagnetic radiation of an antenna can be divided into three regions: evanescent (or reactive near-field), radiating near-field (or Fresnel), and far-field (or Fraunhofer). The boundaries between each region can be estimated through the wavelength (λ) of the source, where from 0 to 3 λ is the evanescent region, from 3 λ to (2D²)/ λ (where *D* is the diameter of the antenna) is the near-field (NF) region, and from (2D²)/ λ to is the far-field (FF) region (Slater 1991). Among these regions, NF measurements are useful for evaluating the radiation from components that can cause electromagnetic interference (Shall *et al.* 2014), characterize devices for NF communications (Liu *et al.* 2023; Nikitin *et al.* 2007) (like radio-frequency identification or NF communication technologies), or for estimating the FF pattern of an antenna using the NF to FF method (Petre and Sarkar 1994), which is possible because the electromagnetic wave travels in a straight line in free space.

Received: 9 Jun 2025 | Accepted: 20 Aug 2025 Peer Review History: Single Blind Peer Review. Section editor: Luiz Martins-Filho



Another application of NF measurements is the characterization of microwave lenses to ensure that their manufacturing is in accordance with the design specifications. Parameters like beam waist and focal length change according to distance, operating frequency, material, and curvature of the lens (Greegor *et al.* 2007; Zarghooni *et al.* 2016). As an emerging technology, a gradient-index lens promises to provide better performance with thinner lenses, but, due to their characteristic of having different indices of refractions according to their thickness, it is also necessary to have a reliable method to characterize them (Chen *et al.* 2023; Roper *et al.* 2014).

Near-field measurements were first performed using an array of antennas (Petre and Sarkar 1994; Yaghjian 1986). Then, new techniques emerged, like a XYZ translational system that moves the NF probe vertically and horizontally (Good *et al.* 2012; Shall *et al.* 2014), or a modern robotic arm (Han *et al.* 2025). Also, to perform the NF to FF conversion, it is necessary to measure the co- and cross-polarization of the antenna (Fig. 1), which requires a bipolar NF probe or the rotation of the NF regular probe (Slater 1991). This setup requires a large space and measures only one planar surface. To measure different planar surfaces, it is necessary to have a third axis to move the antenna perpendicularly to the linear robot system. To perform cylindrical or spherical surface measurements, the antenna must be assembled in a device that contains one or two motors capable of tilting it, and the array of antennas cannot be adapted to such a task (Parini *et al.* 2014; Tanaka *et al.* 2024).



Source: Elaborated by the authors.

Figure 1. Illustration of the (a) co-polarization and (b) cross-polarization measurements.

Some systems use robotic arms to perform NF measurements, but they require modern robotic arms and controllers (Gordon et al. 2015; Hisatake 2022; Lebrón et al. 2016; Novotny et al. 2017), resulting in high costs. A planar surface NF measuring system was developed here using an outdated robotic arm. A computer with a Python routine was used to acquire the electric field measured with a Vector Network Analyzer (VNA). The communication link between the computer and the robotic arm was established with an Arduino Nano. Although this setup requires extra steps to perform the measurement, it is a low-cost system that can measure multiple planar surfaces in a single run. The measured beam waists of microwave lenses for X-, K_u -, K-, and K_a -band showed good agreement with the datasheets, opening possibilities to implement more complex low-cost setups, like cylindrical or spherical scans.

MATERIALS AND METHODS

Equipment

The robotic arm used to move the NF probe is an ABB 2400L series with an S4Cplus controller. The arm follows a script written in RAPID, a programming language from ABB. An Arduino Nano was used to establish a communication between the controller and the computer using the controller's input and output ports. The VNA is used to measure the transmitted S-parameter S_{ij} :

$$S_{ij} = \frac{a_i}{b_j} \tag{1}$$



where a_i is the measured electromagnetic signal at port i, and b_j is the emitted electromagnetic signal from port j. Here, the VNA used was a Keysight PNA-L N5235A that ranges from 10 kHz to 50 GHz. The NF probes were open-ended waveguide probes from Satimo Co., models OEW1000, OEW1800, and OEW2650, covering the frequency ranges from 10 to 15 GHz, 18 to 26.5 GHz, and 26.5 to 40 GHz, respectively. The evaluated antennas under test (AUTs) were focusing lens horn antennas from Anteral, models LHA-F-WR90 (Anteral 2022a), LHA-F-WR62 (Anteral 2022b), LHA-F-WR42 (Anteral 2023), and LHA-F-WR28 (Anteral n.d.). A detailed specification of each antenna is presented in Table 1.

Table 1. Specifications of the focusing lens horn	n antennas used in the measurements.
--	--------------------------------------

Model	LHA-F-WR90	LHA-F-WR62	LHA-F-WR42	LHA-F-WR28
Frequency range (GHz)	8.20-12.40	12.40–180	180-26.50	26.50-40.00
Theoretical focal length* (mm)	181.00	133.75	147.50	146.20
3 dB beam waist, E-plane* (mm)	34.40	23.33	17.80	13.10
3 dB beam waist, H-plane* (mm)	38.68	30.07	22.50	16.90

^{*}At central frequency. Source: Elaborated by the authors based on Anteral (2022a, b, 2023, n.d.).

Measurements parameters

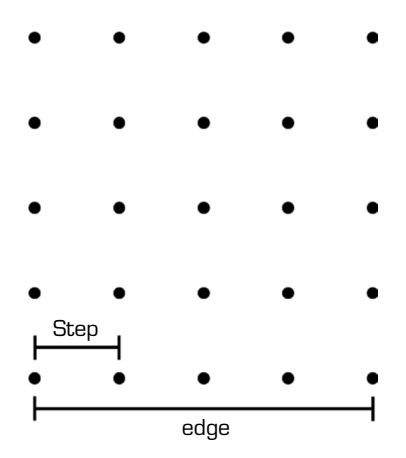
The minimum number of steps between each point was calculated considering the minimum wavelength of the AUT, i.e., the maximum frequency (f_{max}) of the AUT:

$$minSteps = \left\lceil \frac{edge}{\lambda/2} \right\rceil \tag{2}$$

$$\lambda = \frac{f_{max}}{c} \tag{3}$$

where *minSteps* is the rounded-up value of the ratio between the chosen *edge* by half wavelength (λ); $c = 299792458 \text{ m} \cdot \text{s}^{-1}$ is the speed of light in vacuum.

Figure 2 illustrates the concept of edge and step on a 5×5 constellation plane. For each AUT, the edge value was chosen to ensure at least a 10 dB difference from the maximum electrical signal measured at the central point. All measurements started with a distance of 50 mm between the NF probe and the AUT. For multiplane analysis, 20 planes were scanned spaced 1 mm from each other. The parameters used for each multiplane scanning are summarized in Table 2.



Source: Elaborated by the authors.

Figure 2. A 5×5 constellation plane formed by 5 points on each one of the 5 lines. The edge is the full length of the plane and the step is the distance between each point for both X and Y directions.



LHA-F-WR90 LHA-F-WR62 LHA-F-WR42 LHA-F-WR28 X and Y edges (mm) 300.0 200.0 140.0 130.0 Z edge (mm) 300.0 200.0 200.0 200.0 X and Y steps 25.0 25.0 35.0 21.0 Z step 20.0 20.0 20.0 20.0 Lower frequency (GHz) 8.2 12.4 18.0 26.5 Higher frequency (GHz) 12.4 18.0 26.5 40.0 Number of frequency points 31.0 31.0 31.0 31.0

Table 2. Scanning parameters for multiplane measurements.

Source: Elaborated by the authors.

A transverse and a longitudinal scans were also performed to verify the wave propagation in the Z direction. Here, the steps in Z were calculated based on Eq. 2. The parameters used for these analyses are presented in Table 3.

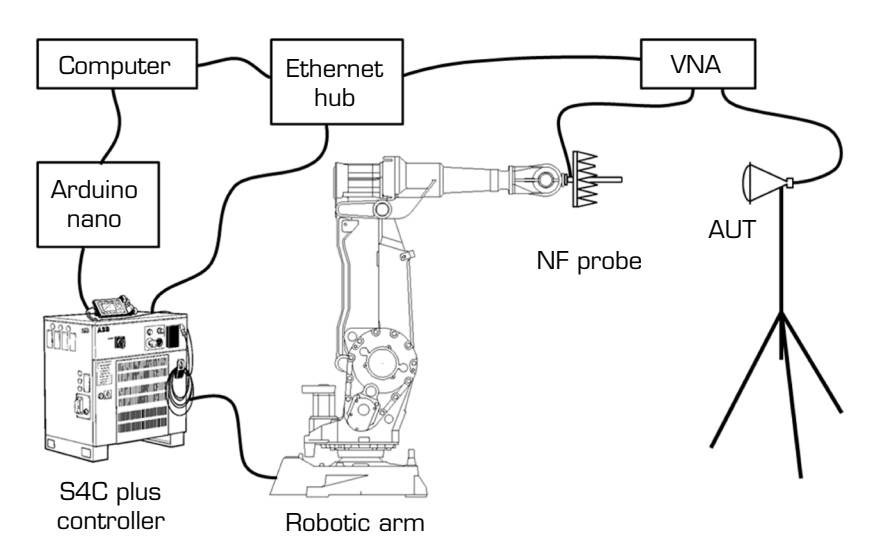
Table 3. Scanning parameters for transverse and longitudinal planes.

	LHA-F-WR90	LHA-F-WR62	LHA-F-WR42	LHA-F-WR28
X or Y edges (mm)	300.0	200.0	140.0	130.0
Z edge (mm)	300.0	200.0	200.0	200.0
X and Y steps	25.0	21.0	25.0	35.0
Z step	25.0	21.0	36.0	54.0
Lower frequency (GHz)	8.2	12.4	18.0	26.5
Higher frequency (GHz)	12.4	18.0	26.5	40.0
Number of frequency points	31.0	31.0	31.0	31.0

Source: Elaborated by the authors.

General overview

An overview of the setup measurement system is presented in Fig. 3. The NF probe is attached to the robotic arm, while the AUT remains stationary on a tripod. The NF probe and the AUT are connected to ports 1 and 2 of the VNA. An Ethernet hub connects the computer, the VNA, and the controller. This connection allows the computer to set up the VNA, acquire data from it, and upload the RAPID routine to the controller via File Transfer Protocol (FTP). Since there is no software to control the robotic arm, an Arduino Nano that indicate the beginning and ending of each movement through the input and output signals of the controller was used.



Source: Elaborated by the authors based on ABB Robotics (2003, 2024).

Figure 3. Schematic draw of the automatized setup.



Computer routines

Since there is no computer software to control the robotic arm directly, the RAPID routine must be uploaded via FTP and executed using ABB's FlexPendant handheld controller. The RAPID routine is programmed to move the NF probe to a center position and wait for an input signal from the Arduino. While the NF probe is centered, the Python routine is initiated in the computer. The Python routine then sends a command to the Arduino via the USB port, triggering the input signal in the controller of the robotic arm. Then, the RAPID routine executes a "for loop," moving the robotic arm to the first point. The output port in the controller triggers a signal in the Arduino, which sends a command to the Python routine. The Python routine then collects the data in the VNA, i.e., it records the transmitted S-parameters as a complex number. Then, the Python routine sends a command to the Arduino that triggers the input signal in the controller and moves the arm to the next position. The communication sequence during scanning is presented in Fig. 4.

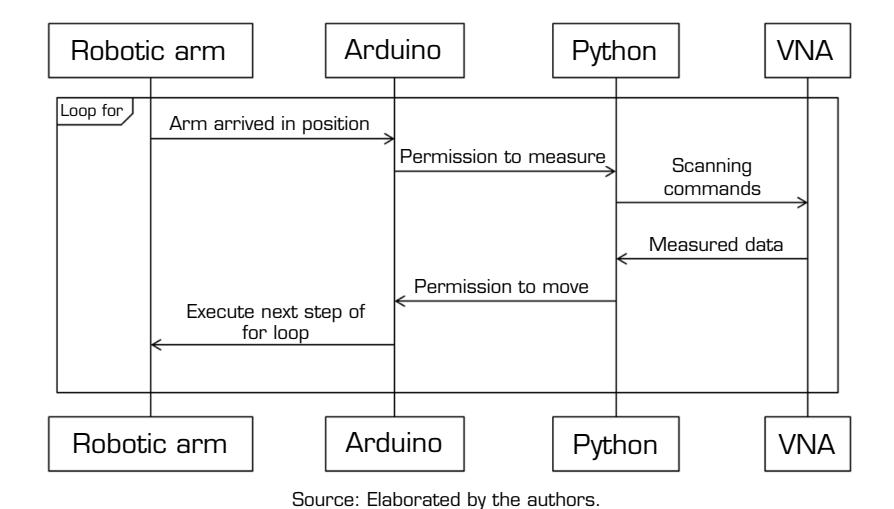


Figure 4. Communication sequence flow chart of the scanning sequence.

The RAPID routine requires some predefined values, such as center position, length of X-, Y-, and Z-edges, the number of steps in each direction, orientation, and axes configuration. Thus, the NF probe must be centrally aligned with the AUT. The position and quaternions to be inserted in the RAPID routine must be manually verified in the FlexPendant. The co-polarization is set as 0° , and the cross polarization is set as 90° . A variable direction (dir) defines whether the movement will be left-to-right (dir = 1) or right-to-left (dir = -1), thus performing a raster scan. After initiation, each step distance is calculated as:

$$xStep = \frac{xEdge}{points_{max} - 1} \tag{4}$$

$$yStep = \frac{yEdge}{lines_{max} - 1} \tag{5}$$

$$zStep = \frac{zEdge}{planes_{max}}.$$
 (6)

Each movement uses a combination of the MoveL and RelTool functions (ABB Robotics 2010), which move the probe linearly (MoveL) to a new position calculated relative to the central point (RelTool). The first movement is to the center, i.e., the RelTool parameters are the central position, x = 0, y = 0, and z = 0. Then, the displacement variables in x and y are calculated, defining the new position that the MoveL function will perform. The direction is also calculated, and then the robotic arm moves to the first point.



Here, the RAPID routine executes the "for loop," which scans throughout the line. Then, the robotic arm is moved up and scans the whole line again, but this time in the opposite direction. Each line consists of n points, i.e., each line is discretized in n steps. This is done over the entire plane (the discretized XY square), and is defined as the 'Scan' procedure in the RAPID routine. Since the 'Scan' procedure is independent of the main procedure, scanning multiple planes with co- and/or cross-polarizations is easy. For example, if it is desirable to scan two planes with co- and cross-polarization, the routine would perform the 'Scan' procedure first, reset x and y values, set pol = 90, perform the Scan procedure again, move to the next plane setting pol = 0 and repeat the Scan procedure for pol = 0 and pol = 90 again. Figure 5 illustrates the RAPID routine to scan multiple planes with co- and cross-polarization.

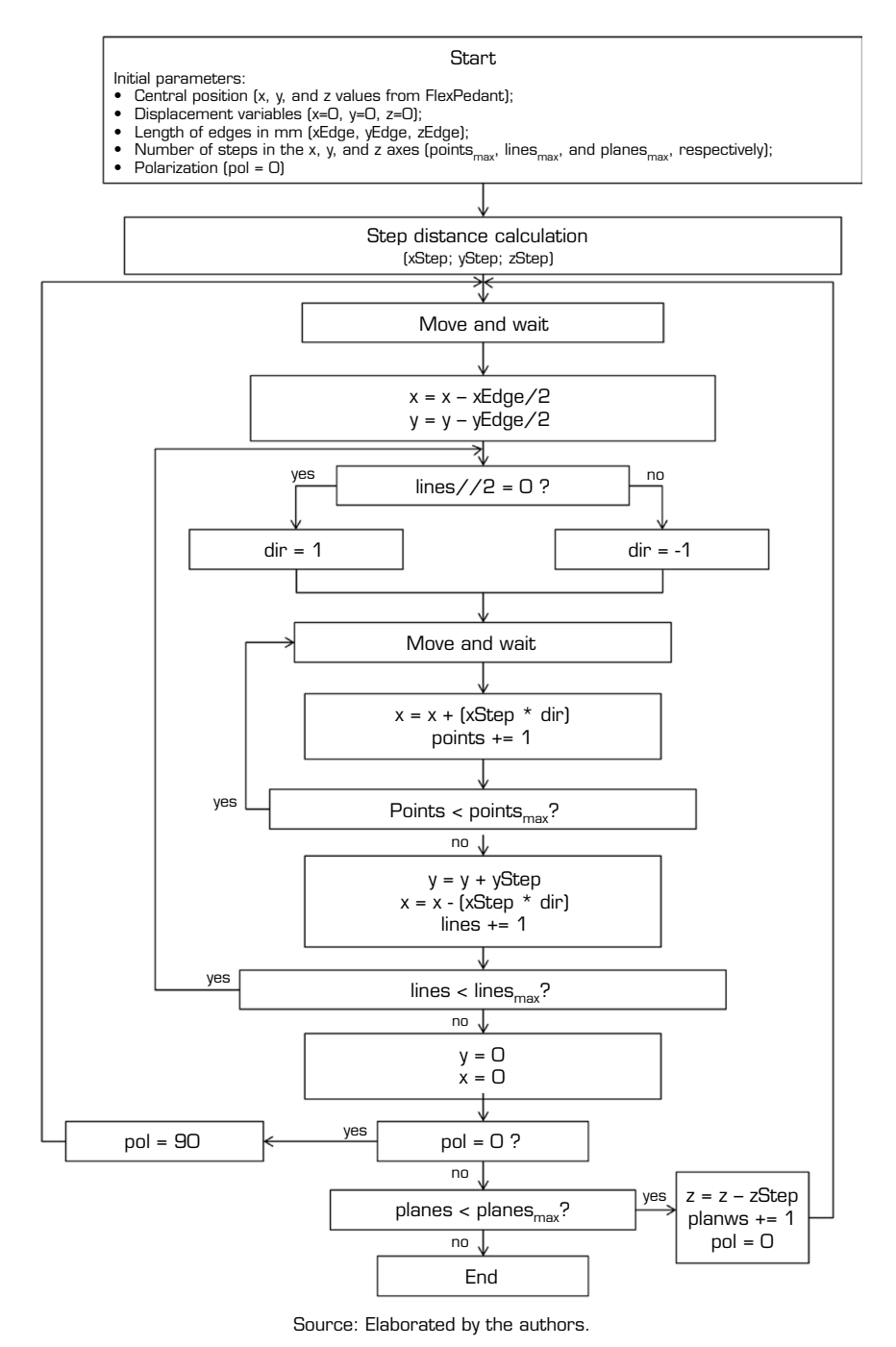


Figure 5. Flow chart of the RAPID routine that executes co- and cross-polarization measurements of multiple planes.



The Python routine that communicates with the VNA and Arduino is under trade secret and cannot be published. All variables are input into the routine, including the RAPID variables already discussed and the VNA variables, such as frequency range, number of frequency points, average, power, and so on. This information is used to set up the VNA, to create the RAPID routine, and to generate the report later. The Python routine is started after uploading and initiating the RAPID routine. The first command configures the VNA with the desired parameters. Since the robotic arm should be centralized and aligned with the AUT, the Python routine asks to perform normalization. The normalization is optional; after this step, the routine sends a command to the Arduino to move the robotic arm to the first point, as previously explained. After receiving the signal from the Arduino indicating that the robotic arm is in position, the Python routine sends a command to the VNA to execute the measurement. The VNA returns the S-parameters as a complex number, which is stored in the dynamic memory along with the calculated position. Finally, the Python routine sends a command to the Arduino to move the arm to the next point. After scanning the whole plane, the Python routine saves the stored info into a text file. The routine allows the rotation of the probe by 90° to perform a cross-polarized scan of the same plane. These scans can be automatically performed over several planes, with the robotic arm moving backwards. A simplified flow chart of the Python routine is presented in Fig. 6.

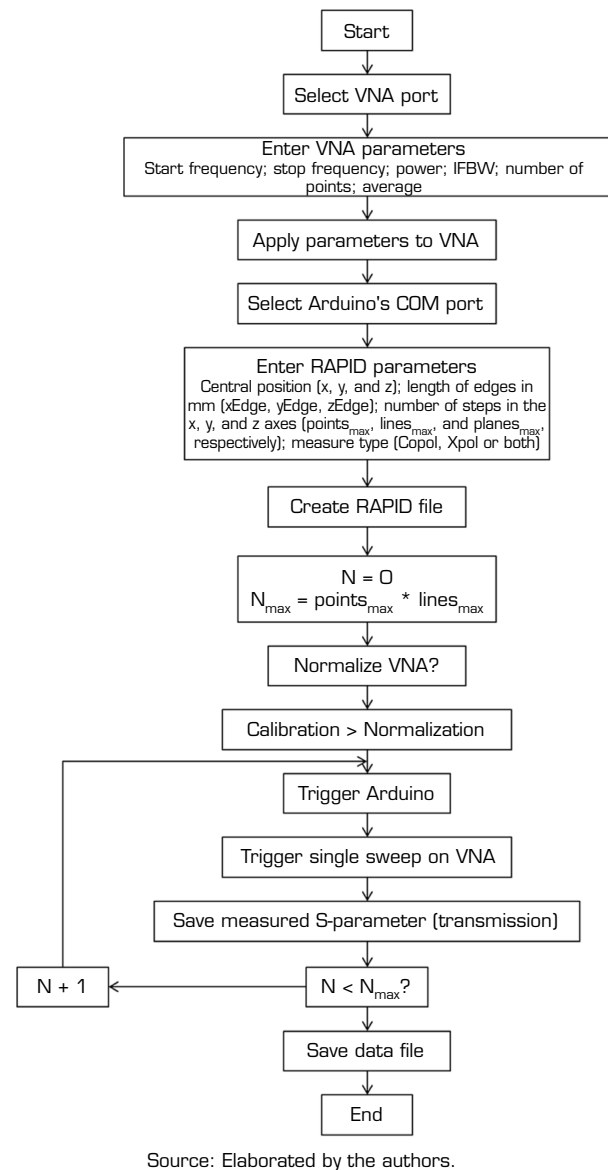


Figure 6. Simplified Python routine flow chart.



When all planes are measured, the Python routine presents an end message, and the robotic arm remains at the central position of the last plane, awaiting manual deactivation.

Post-processing routine

After generating the files for all planes, the data undergoes a post-processing routine in Python that creates a 2D color map of each plane. This routine is available on GitHub (see Data Availability Statement), along with the measured data of all microwave lenses.

The routine extracts information, such as the distance from the probe to the AUT, the edges lengths, and the number of points, lines, and planes. It can import a single plane file or multiple planes files as a Pandas DataFrame. After importing the plane, the magnitude and phase are calculated. A normalized magnitude is calculated for each plane, since it may be difficult to ensure the exact position of the higher amplitude when measuring. It is possible to calculate a normalized magnitude over all planes if multiple planes were imported. Each plane is plotted as a 2D color map considering the normalization over all planes.

There are two subroutines to verify the electromagnetic wave propagation. The first one is the cutPlane subroutine, which considers the measurements of all planes and acquires the values from the desired location (the central cut is considered at 0 mm). It performs a horizontal (or vertical) cut across all measured planes. The plotPlane subroutine is used to plot XZ (or YZ) plane exclusively, since it is a single data file containing the longitudinal (or transverse) plane measured with a slight modification of the RAPID routine. The horizontal cut and the longitudinal measurement are related to the H-plane, while the vertical cut and transverse measurement are related to the E-plane.

RESULTS AND DISCUSSION

The results presented here are reduced in the number of planes and frequencies to provide an easier understanding of the electromagnetic behavior of the traveling wave. Three different planes and frequencies were chosen for each lens, representing the front, middle, and back planes. The chosen middle plane was the closest one to the focal length in the datasheet at the central frequency.

Two measurements were performed for each microwave lens. The first measurement considered the minimum calculated distance for XY following the Nyquist principle, but with only 20 planes for each AUT to reduce the scanning time, especially for higher frequency lenses. To check if 20 planes would result in a significant error when plotting the XZ and YZ cuts, transverse and longitudinal scans were performed with a finer resolution.

X-band

The first set of results is for the X-band lens (LHA-F-WR90), described in Fig. 7, where the XY planes 0, 9, and 19 are plotted at 8.2, 10.3, and 12.4 GHz. For the X-band lens, the focal length at 10.3 GHz is 181.00 mm (Anteral 2022a), and plane 9 is at 192.11 mm. The solid black line circle surrounds –10 dB magnitude, while the yellow one surrounds –3 dB.

Table 4 shows the size of the E-plane and H-plane -3 dB beam waists plotted in Fig. 7. Since planes 0 and 19 were beyond the -3 dB focal point, the spot sizes were 0 mm for all frequencies. An interpolation of the measured data was performed to better estimate the size of E- and H-planes. Based on these values, the -3 dB beam waist at a distance of 192.11 mm is 31.23 mm in the E-plane and 38.44 mm in the H-plane, measured at 10.3 GHz. The datasheet presents an E-plane of 34.40 mm and an H-plane of 38.68 mm at 181.0 mm, measured at the central frequency. It is a difference of 3.17 mm and 0.24 mm for E- and H-plane, respectively, considering an 11.11 mm difference between focal lengths.

Figure 8 shows the vertical and horizontal cuts of all 20 planes, representing the E- and H-planes over the Z-axis, respectively. The focal length at middle frequency starts at \sim 90 mm and goes up to \sim 300 mm, considering that the focal length is the region with magnitude above -3 dB. The datasheet provides that the focal length distance goes from \sim 155 up to \sim 195 mm from 8.2 to 12.4 GHz. Through Fig. 8, it is possible to see that this range from 150 to 200 mm is a safe region, where the beam waist will always have -3 dB. It also shows that the vertical cut (E-plane) is slightly thinner than the horizontal cut (H-plane), which is coherent with the datasheet. (Table 4)



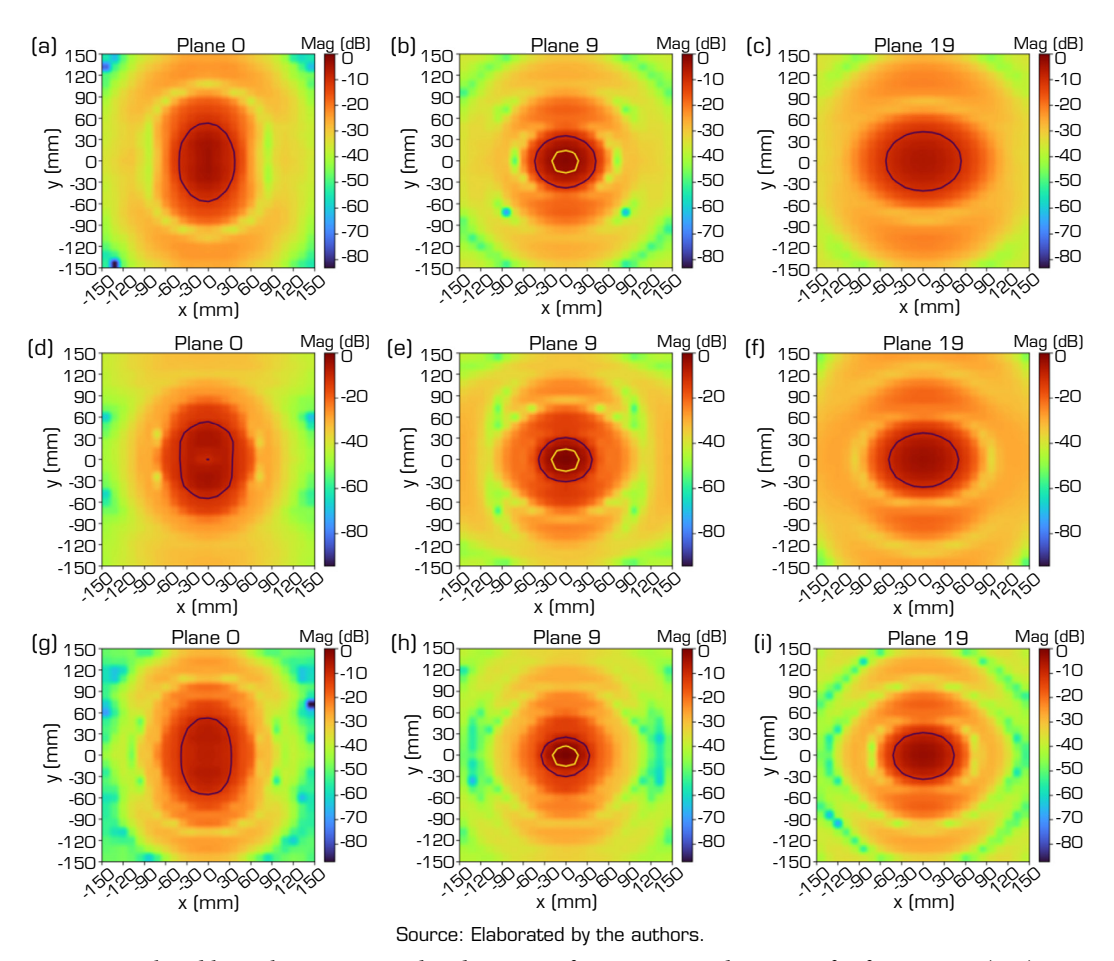


Figure 7. X-band lens planes measured at distances of 50, 192.11, and 350 mm for frequencies (a–c) 8.2, (d–f) 10.3, and (g–i) 12.4 GHz, respectively.

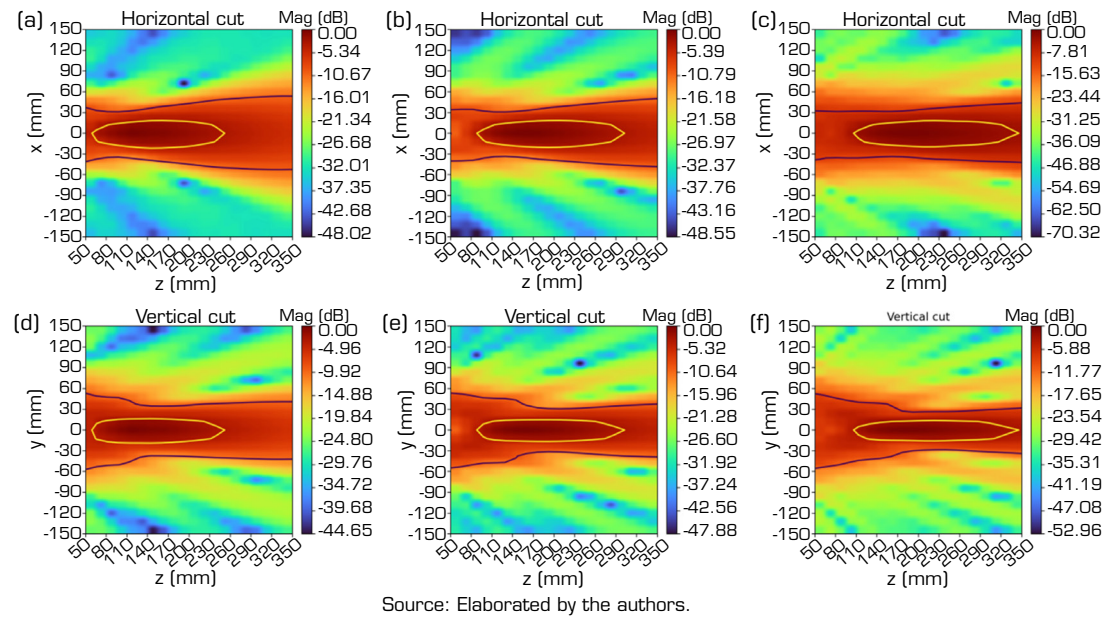


Figure 8. Horizontal cuts at (a) 8.2, (b) 10.3, and (c) 12.4 GHz and vertical cuts at (d) 8.2, (e) 10.3, and (f) 12.4 GHz of the 20 XY planes plotted in Fig. 7.



Plane O Plane 9 Plane 19 50.00 mm 192.11 mm 350.00 mm E (mm) H (mm) E (mm) H (mm) E (mm) H (mm) 8.20 GHz 0.00 0.00 31.23 36.94 0.00 0.00 10.30 GHz 0.00 0.00 31.23 38.44 0.00 0.00 12.40 GHz 0.00 0.00 28.23 36.04 0.00 0.00

Table 4. The -3 dB beam waist calculated from the X-band measured planes.

Source: Elaborated by the authors.

Figure 9 presents the measured longitudinal and transverse planes equivalent to the horizontal and vertical cuts of Fig. 8. The longitudinal and transverse measurements are very similar to the cut planes because the Z-step is equal to 25, while the total number of XY planes was 20. This means that the quantity of XY planes almost covered the finer resolution to investigate the focal length. It can be noticed some small differences in the beam spread of Fig. 9e and f after 230 mm, probably because the maximum value measured was different between analyses.

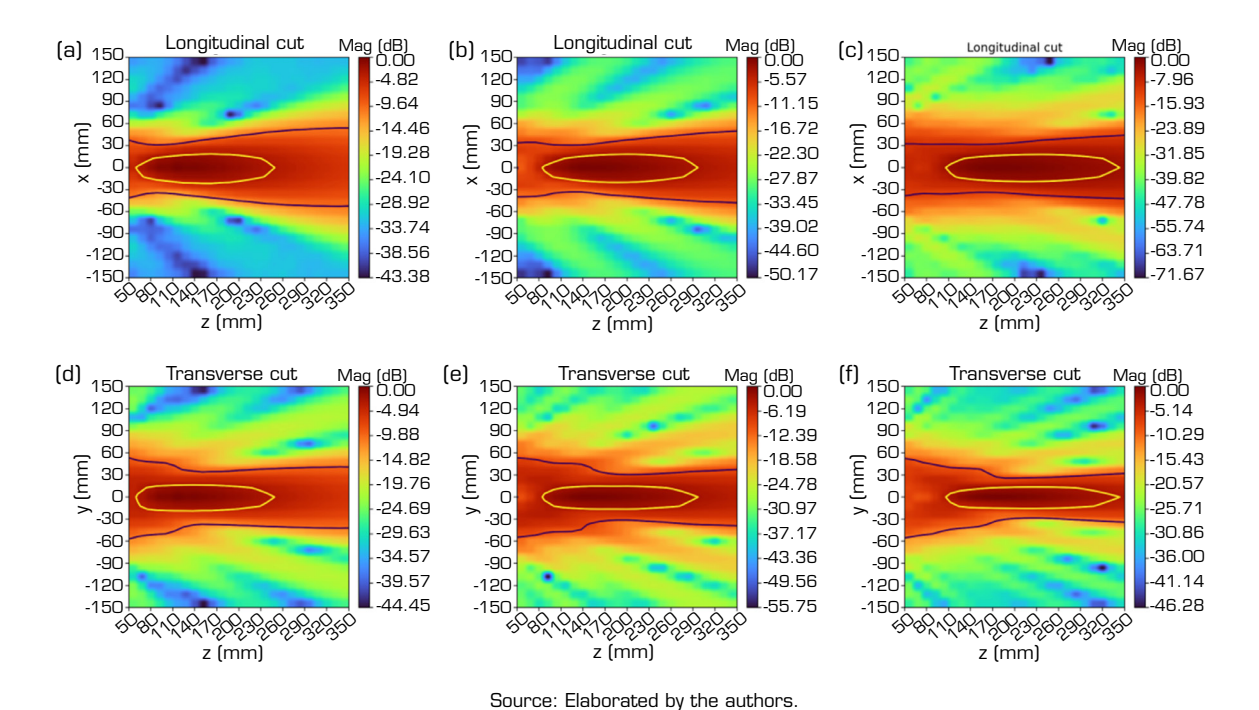


Figure 9. Measured longitudinal cuts at (a) 8.2, (b) 10.3, and (c) 12.4 GHz and transverse cuts at (d) 8.2, (e) 10.3, and (f) 2.4 GHz of the X-band lens with 25 steps in the Z-axis.

K,,-band

For the K_u -band lens (LHA-F-WR62), the 8th XY plane is at 134.21 mm, which is the closest middle plane based on the distance given in the datasheet (133.75 mm at 15.2 GHz) (Anteral 2022b). Figure 10 shows the front, middle, and back planes at 12.4, 15.2, and 18.0 GHz. The ellipses formed by the -10 dB magnitude contour (black solid lines) are more accentuated, illustrating better the E- and H-planes differences between front and back planes. Also, Fig. 10d shows two circles of -3 dB magnitude (yellow solid line), almost like two poles. This is a lens aberration (Bachynski and Bekefi 1956) caused by the proximity of the NF probe to the AUT. By comparing the -3 dB contour at the central frequency (Fig. 10b, e, and h), it is evident that the beam waist decreases as the frequency increases.



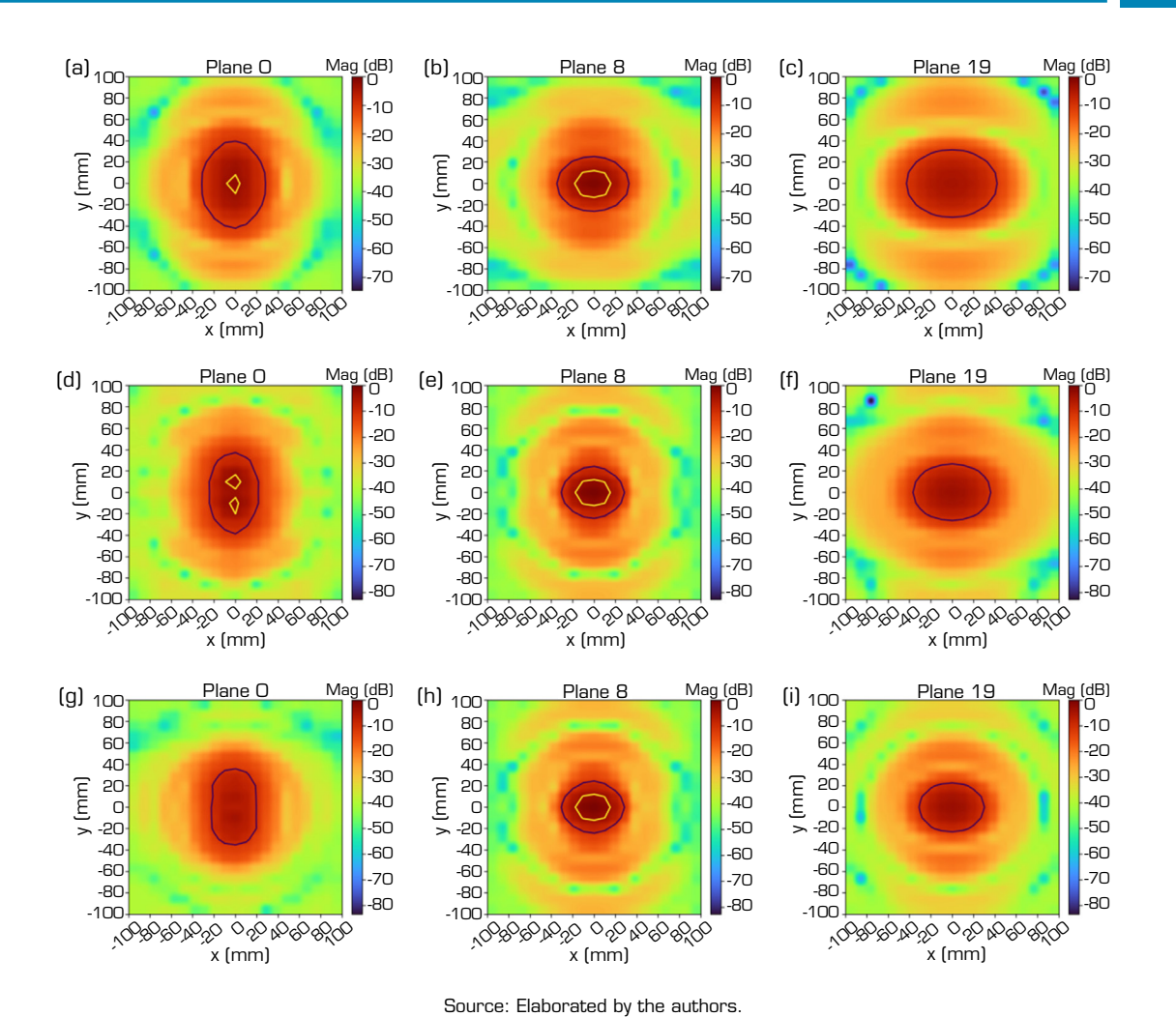


Figure 10. K₁₁-band lens planes at 50 mm, 134.21 mm, and 250 mm at (a-c) 12.4, (d-f) 15.2, and (g-i) 18.0 GHz, respectively.

Table 5 summarizes the sizes of the E- and H-planes of the plots in Fig. 10. Similarly to the X-band results, some spot sizes are 0 mm because the planes do not present values higher than -3 dB. The -3 dB beam waist at 10.3 GHz measured at 134.21 mm distance is 24.04 mm for the E-plane and 32.43 mm for the H-plane. The datasheet presents an E-plane of 23.33 mm and an H-plane of 30.07 mm at 133.75 mm and at the central frequency. The two circles presented in Fig. 10d measured 36.34 mm in the E-plane from one edge to another, while the H-plane is 0 mm, as the horizontal measurement is taken at the center of the image, where the values are below -3 dB.

Table 5. The -3 dB beam waist calculated from the K_u -band measured planes.

	Plane 0		Plar	ne 8	Plan	e 19
	50.0	D mm	134.21 mm		250.00 mm	
	E (mm)	H (mm)	E (mm)	H (mm)	E (mm)	H (mm)
12.40 GHz	17.12	12.31	24.62	33.63	0.00	0.00
15.20 GHz	36.34*	0.00	24.04	32.43	0.00	0.00
18.00 GHz	0.00	0.00	20.72	24.62	0.00	0.00

*Considering the two circles presented. Source: Elaborated by the authors.

The aberration in Fig. 10d is clearer when looking at the vertical cut of Fig. 11e. Also, Fig. 11f presents a small aberration around 70 mm regarding the -3 dB contour. These aberrations are far from the defined focal length range established in the datasheet, which ranges from \sim 115 to \sim 142 mm at central frequency.



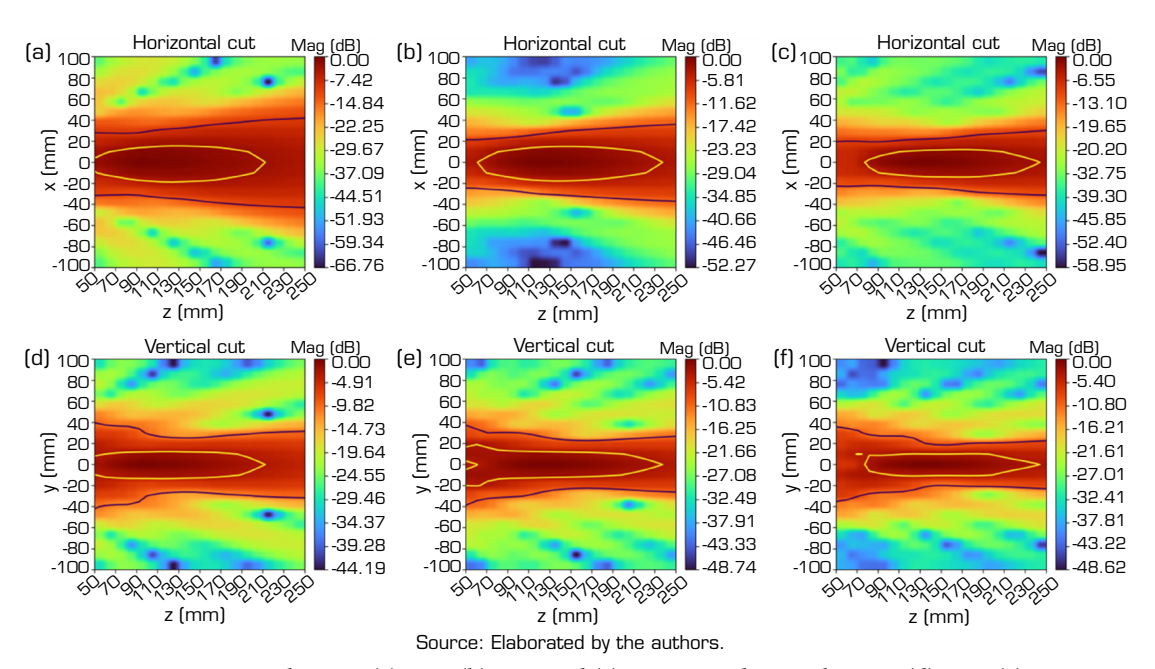


Figure 11. Horizontal cuts at (a) 12.4, (b) 15.2, and (c) 18 GHz and vertical cuts at (d) 12.4, (e) 15.2, and (f) 18 GHz of the 20 XY planes plotted in Fig. 10.

The longitudinal and transverse measurements (Fig. 12) have a Z-step equals to 21, which is almost the same number of XY planes used in Fig. 11. This extra plane provides more details about the aberration at the beginning of the E-plane at 15.2 GHz but the disturbance in the E-plane at 18 GHz (Fig. 12f) is almost imperceptible, meaning that a better resolution may reduce such errors. Similarly to the X-band, the beam spread in Fig. 12f is slightly different after 190 mm distance, but the main focal beams are identical, even with the sharp ending.

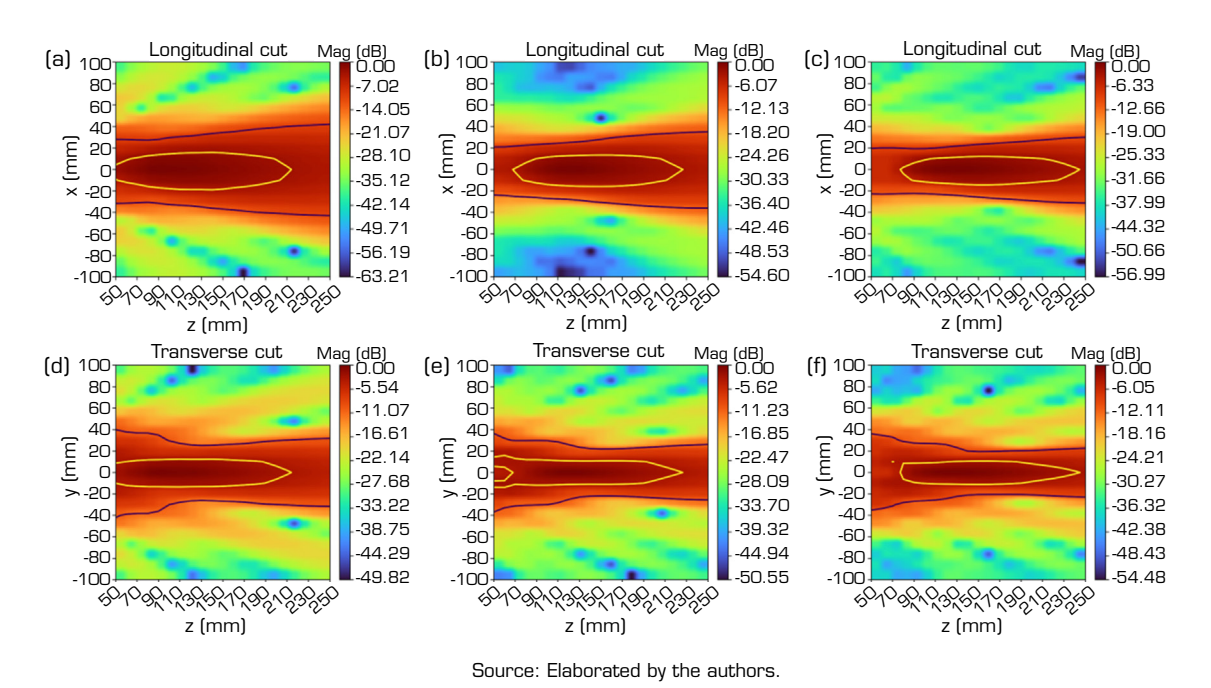


Figure 12. Measured longitudinal cuts at (a) 12.4, (b) 15.2, and (c) 18 GHz and transverse cuts at (d) 12.4, (e) 15.2, and (f) 18 GHz of the K_u-band lens with 21 steps in the Z-axis.



K-band

The central frequency of the K-band lens (LHA-F-WR42) is 22.25 GHz. At this frequency, the focal length in the datasheet is at 147.50 mm (Anteral 2023). The closest XY plane to this distance is plane 9, which is at 144.74 mm from the AUT. Figure 13 presents the front, middle, and back planes at 18.00, 22.25, and 26.50 GHz. The front plane at 18 GHz (Fig. 13a), has two –3 dB circles aberration. Although almost imperceptible, some effects caused by the aberration at other frequencies can be noticed as well (the red shades inside the –10 dB limit in Fig. 13d and g). At 144.74 mm distance, the focus beam become smaller at higher frequencies (Fig. 13b, e, and h). The back planes show an opposite behavior, with the beam width increasing with the increasing frequency (Fig. 13c, f, and i).

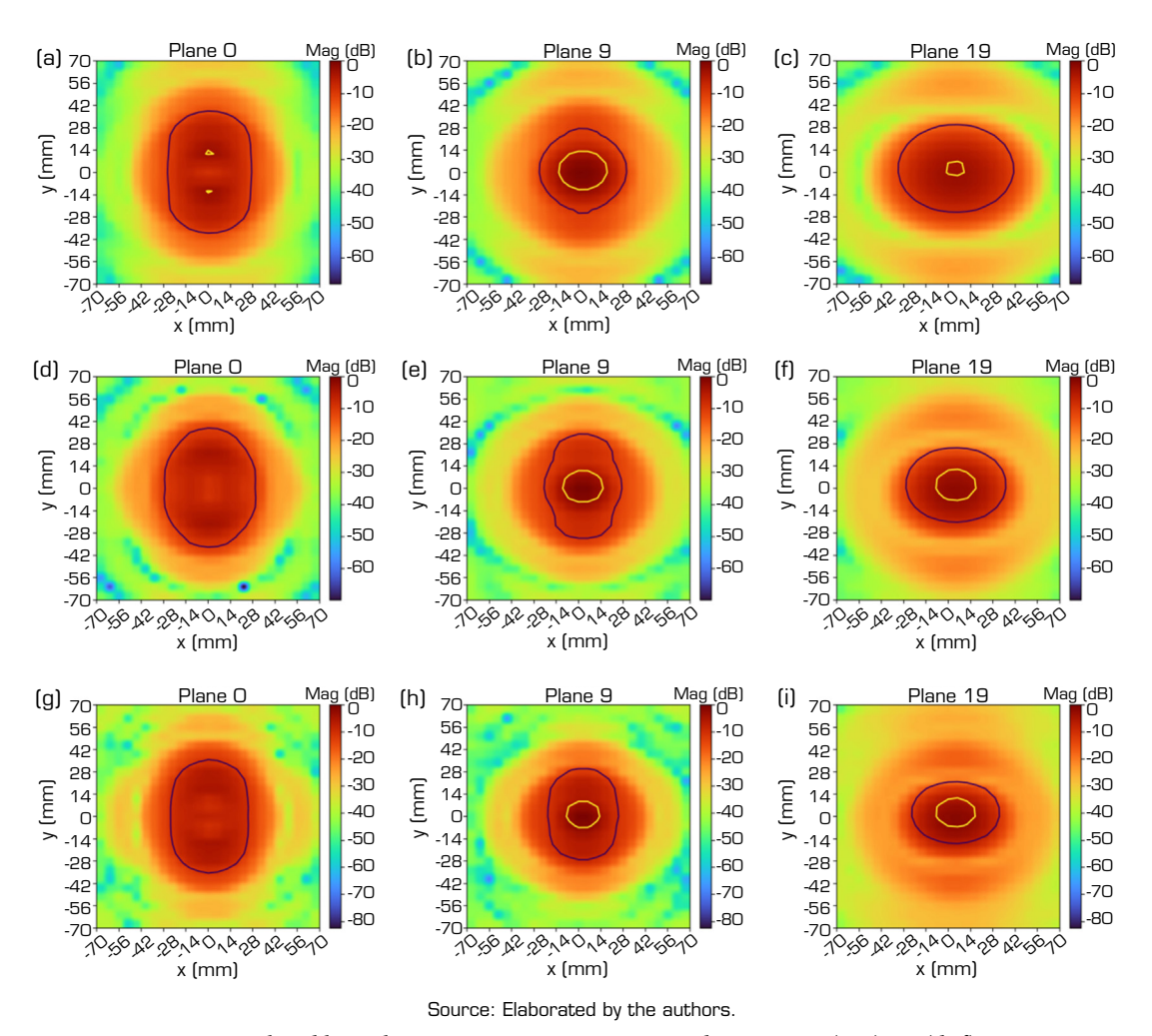


Figure 13. K-band lens planes at 50 mm, 144.74 mm, and 250 mm at (a–c) 18, (d–f) 22.25, and (g–i) 26.5 GHz, respectively.

Table 6 shows the E- and H-planes of the beam waists plotted in Fig. 13. The -3 dB magnitude beam waist at a distance of 144.74 mm is 19.22 mm for the E-plane and 24.92 mm for the H-plane, measured at 22.25 GHz. The datasheet shows that the E-plane is 17.8 mm and the H-plane is 22.5 mm at 147.5 mm and 22.25 GHz. This is a difference of 1.42 mm for the E-plane and 2.42 mm for the H-plane, with the central distance difference of 2.76 mm. Figure 13a shows two -3 dB circles. The beam waist, measured from edge to edge, is 26.43 mm in the E-plane, while the H-plane beam waist is 0 mm, as the horizontal measurement is taken at the center of the plot. Additionally, plane 0 shows no values above -3 dB for 22.25 and 26.50 GHz, indicating that the focal spot lies beyond this distance for these frequencies.



	Plane 0		Plai	ne 9	Plan	e 19
	50 mm		144.74 mm		250 mm	
	E (mm)	H (mm)	E (mm)	H (mm)	E (mm)	H (mm)
18.0 GHz	26.43*	0	23.72	30.03	6.61	10.81
22.25 GHz	0	0	19.22	24.92	18.02	24.92
26.5 GHz	0	0	16.22	20.42	16.52	24.02

Table 6. The -3 dB beam waist calculated from the K-band measured planes.

The aberrations close to the lens can be better visualized in Fig. 14. Here, horizontal aberrations are presented as well, not only the vertical ones like in the K_u frequency band. The -3 dB limit shows that the focal length region can go from \sim 70 mm at 18 GHz to beyond 250 mm at 26.5 GHz. Although the contour looks out of range, the datasheet established a focal length distance between \sim 135 and \sim 155 mm for the whole frequency range.

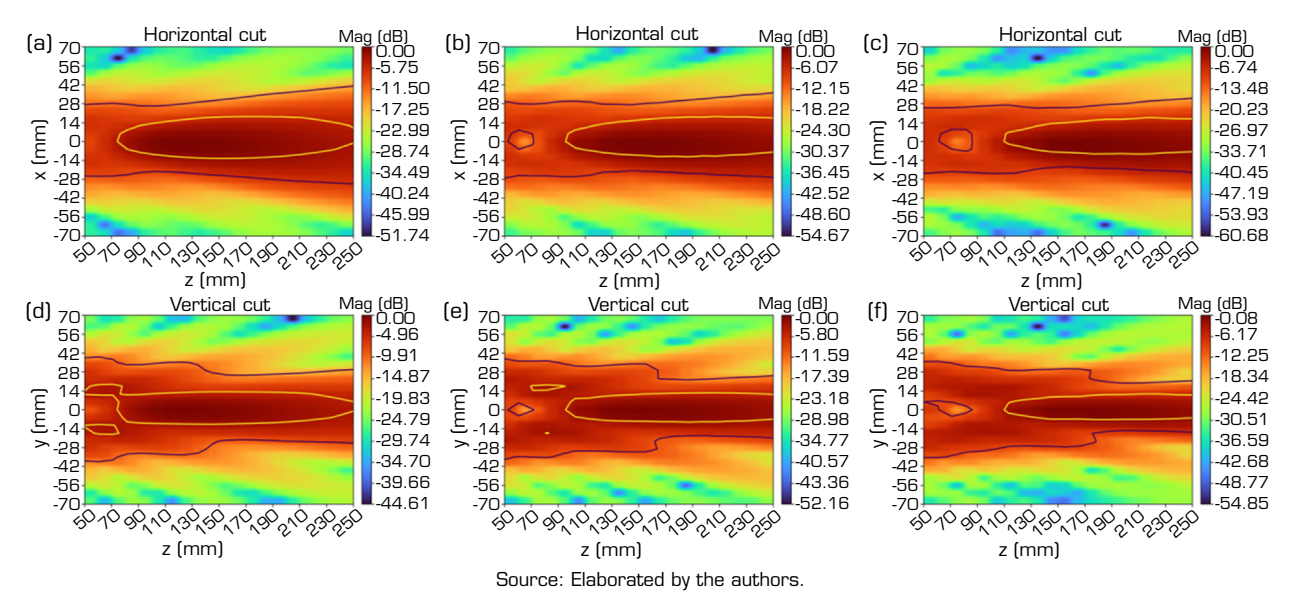


Figure 14. Horizontal cuts at (a) 18, (b) 22.25, and (c) 26.5 GHz and vertical cuts at (d) 18, (e) 22.25, and (f) 26.5 GHz of the 20 XY planes plotted in Fig. 13.

The longitudinal and transverse scans performed with a better resolution are presented in Fig. 15. The results are very similar despite the higher resolution of 36 steps in the Z-axis. Figure 15f presents some regions with magnitude above -3 dB around 100 mm that are not presented in Fig. 2f. Because of the higher resolution, the aberrations at distances close to the AUT are more detailed, but the focal length remains almost the same. It is interesting to note that the longitudinal focal length for the lower frequency starts at \sim 80 mm, while it starts at \sim 110 mm for the higher frequency. This is because the frequency range of the K-band is 8.5 GHz, which is larger than the previous frequency bands and pushes the beginning of the focal length further in distance. Although the focal length of higher frequencies goes beyond 250 mm, the focal length of the lowest frequency ends at this distance. It becomes clear that the beginning of the focal length is defined by the highest frequency, while the ending is defined by the lower frequency.

K_a-band

Since it was defined that all measurements should start at a 50 mm distance from the AUT, the aberrations in the first plane of the K_a -band lens (LHA-F-WR28) are more visible due to its higher frequency range. The focal length at central frequency (33.25 GHz) provided in the datasheet is 146.20 mm (Anteral n.d.), and the closest XY plane to this distance is plane 9, at 144.74 mm. At this distance, the beam waist becomes smaller with the increasing frequency (Fig. 16b, e, and h). It is interesting to notice that the pattern of the -10 dB magnitude is not just an ellipse due to the proximity to the AUT. At the back plane (Fig. 16c, f, and i), the patterns become regular, with the beam waist increasing with increasing frequency.



^{*}Considering the two poles presented. Source: Elaborated by the authors.

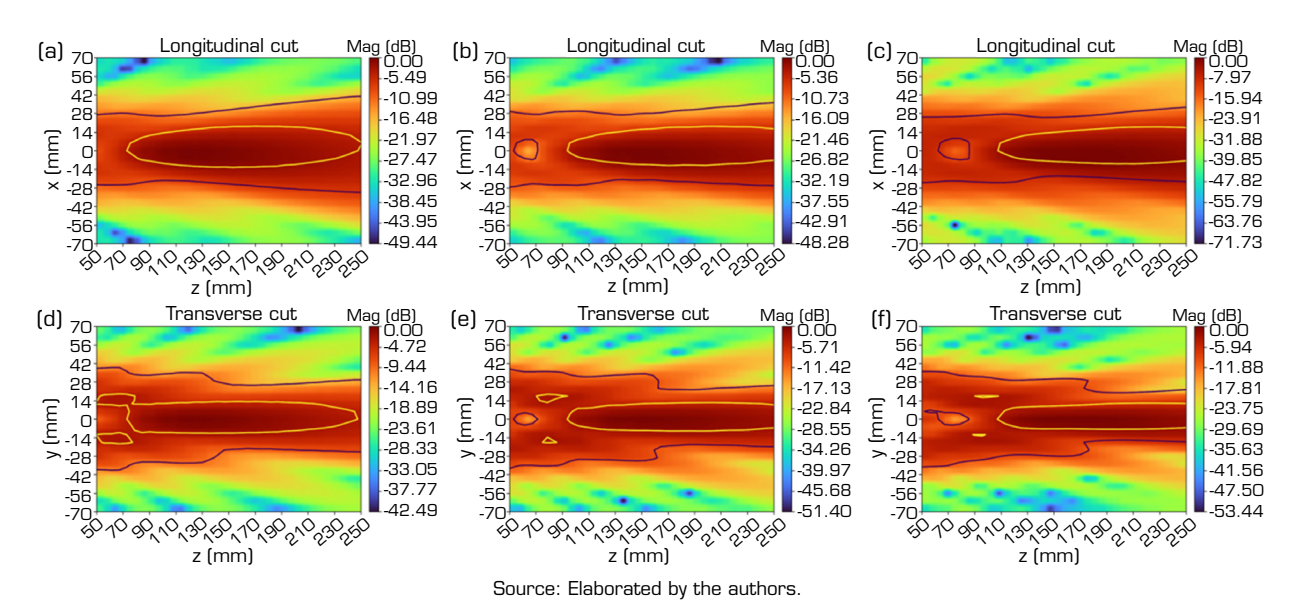


Figure 15. Measured longitudinal cuts at (a) 18, (b) 22.25, and (c) 26.5 GHz and transverse cuts at (d) 18, (e) 22.25, and (f) 26.5 GHz of the K-band lens with 36 steps in the Z-axis.

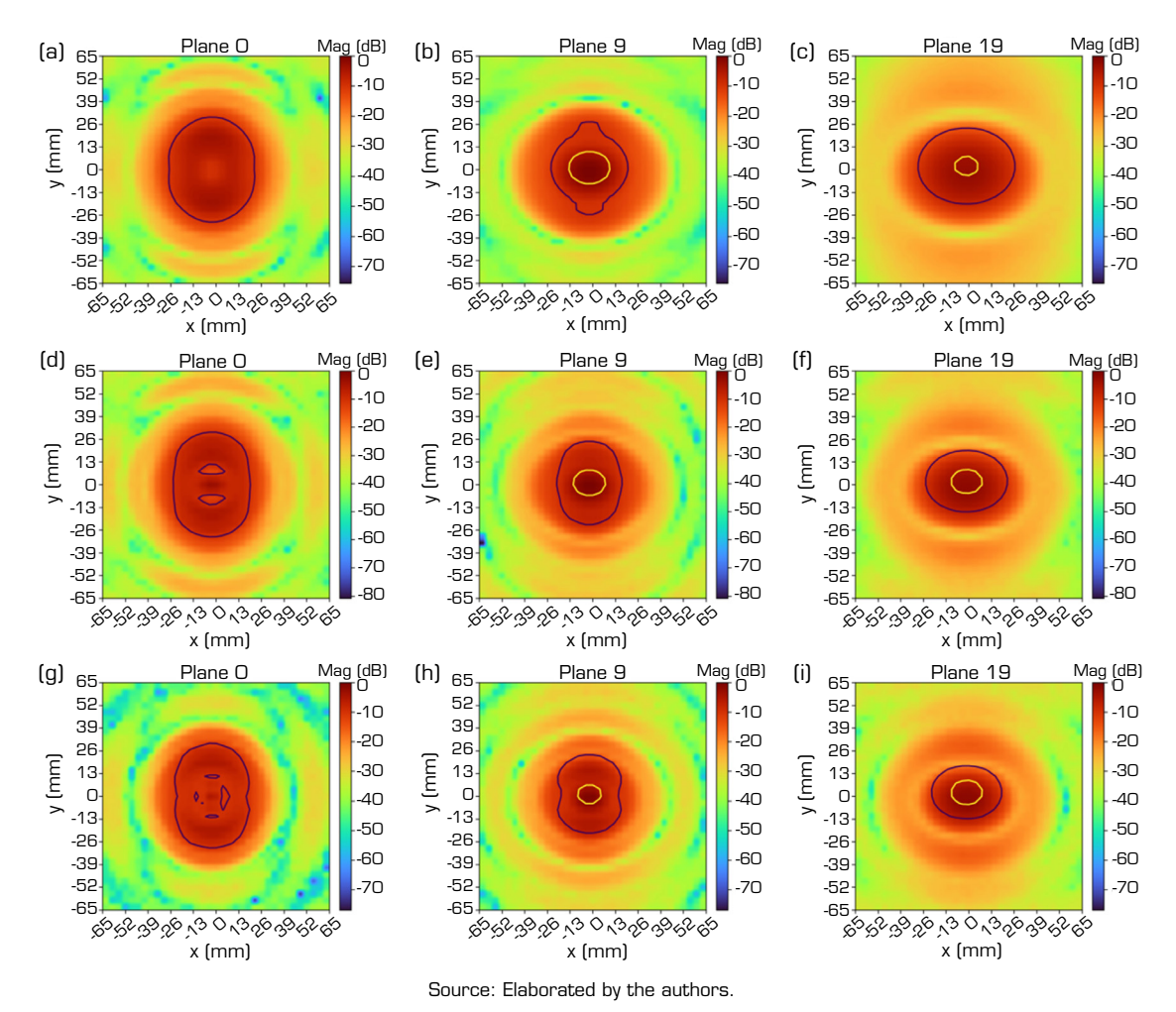


Figure 16. K_a-band lens planes at 50 mm, 144.74 mm, and 250 mm at (a-c) 26.5, (d-f) 33.25, and (g-i) 40 GHz, respectively.



Table 7 shows the sizes of the E- and H-planes of the plots in Fig. 16. Plane 0 has no magnitude above –3 dB, resulting in spot sizes of 0 mm. The –3 dB beam waists at 144.74 mm are 14.11 and 18.02 mm for the E- and H-planes, measured at 33.25 GHz. The beam waists of E- and H-planes in the datasheet at 146.2 mm are 13.1 and 16.9 mm, respectively. With a difference of 1.46 mm between plane 9 and the focal distance in the datasheet, the E- and H-planes beam waists have a difference of 1.01 and 1.12 mm.

Table 7. The –3 dB beam waist c	lculated from the	K _a -band measured planes.
--	-------------------	---------------------------------------

	Plane 0		Plane 0 Plane 9		Plane 19	
	50 mm		144.74 mm		250 mm	
	E (mm)	H (mm)	E (mm)	H (mm)	E (mm)	H (mm)
26.5 GHz	0	0	17.72	22.82	10.81	12.31
33.25 GHz	0	0	14.11	18.02	13.21	17.12
40.0 GHz	0	0	10.51	13.21	13.51	17.12

Source: Elaborated by the authors.

Figure 17 shows the horizontal and vertical cuts where the NF aberrations are more visible, especially at higher frequencies. It is important to mention that some –10 dB limit lines, like the circle vertically centered at 50 mm in Fig. 17a, refer to a small part that is actually below –10 dB and therefore must not be confused with a limit line encompassing a higher magnitude. Also, this analysis more clearly shows that the limit lines look misplaced from the color map. This happens because the 2D color maps pass through an interpolation to become smoother, while the limit lines are traced based on the actual data.

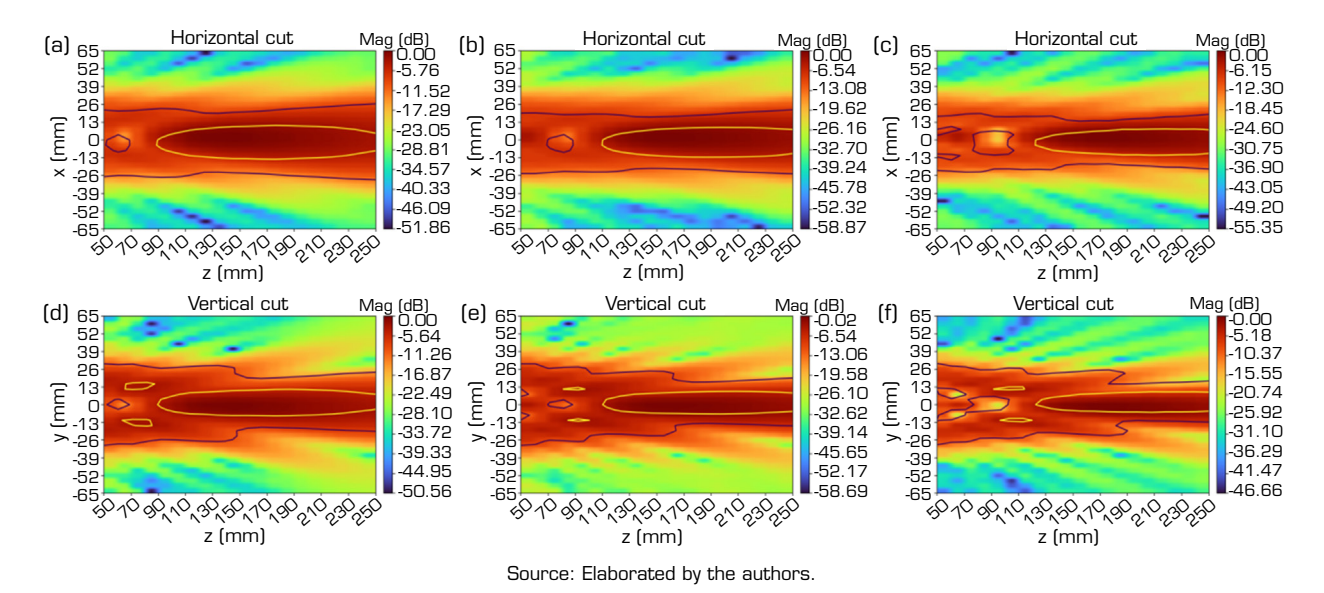


Figure 17. Horizontal cuts at (a) 26.5, (b) 33.25, and (c) 40 GHz and vertical cuts at (d) 26.5, (e) 33.25, and (f) 40 GHz of the 20 XY planes plotted in Fig. 16.

A higher resolution on the Z-axis (Fig. 18) shows that the vertical and horizontal cuts are close to the transverse and longitudinal measurements. Using zStep = 54 shows that a higher resolution brings the color map values close to the actual measured data, i.e., the colors above -10 dB are better limited by the black solid lines of the data. Also, the focal length here is more limited than in the K-band, since the frequency range encompasses 13.5 GHz. At 40 GHz (Fig. 18c and d), aberrations are much more visible.

Table 8 summarizes all beam waists at central frequencies of E- and H-planes, as well as the focal distance provided in the datasheets and the closest planes. The difference between experimental and theoretical values is very close to each other, with a maximum difference of 3.17 mm for the E-plane of the X-band.



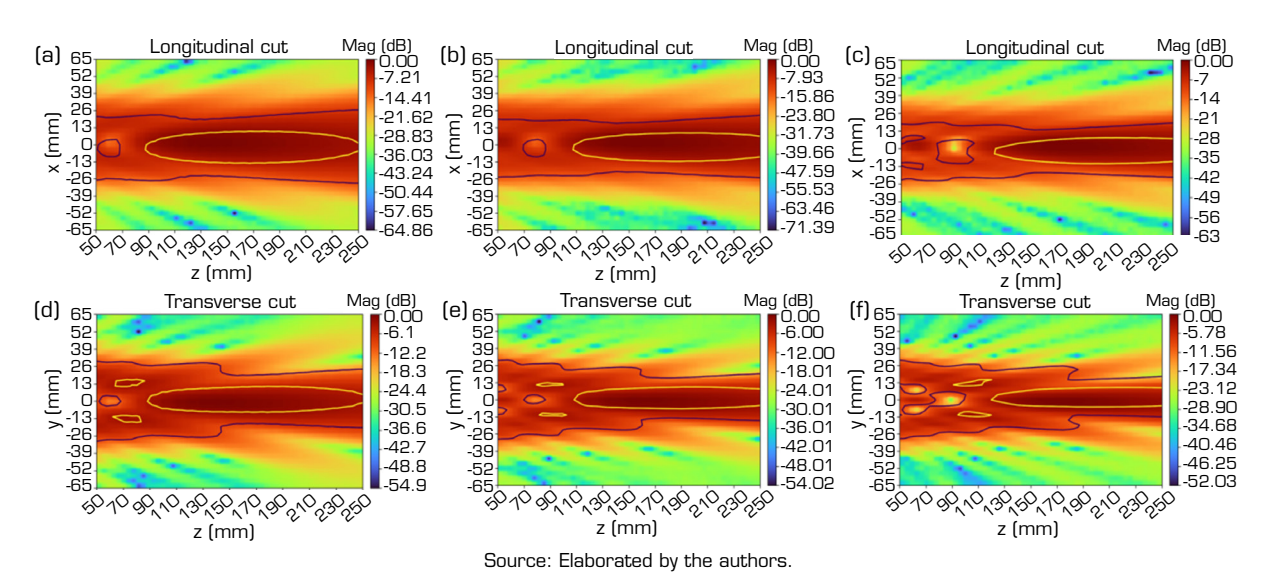


Figure 18. Measured longitudinal cuts at (a) 26.5, (b) 33.25, and (c) 40 GHz and transverse cuts at (d) 26.5, (e) 33.25, and (f) 40 GHz of the K_a-band lens with 54 steps in the Z-axis.

Table 8. Comparison of theoretical and measured focal distance and beam waist for all lenses. The difference between these values is presented as well, showing that the values are very close to each other.

	Facal distan		Beam wa	aist (mm)
	rocai distai	Focal distance* (mm)		Н
	Theoretical	181.00	34.40	38.68
X-band (10.30 GHz)	Measured	192.11	31.23	38.44
(10.00 0112)	Difference	11.11	-3.17	-0.24
	Theoretical	133.75	23.33	30.07
K _u -band (15.20 GHz)	Measured	134.21	24.02	32.43
(10.20 0112)	Difference	0.46	0.69	2.36
	Theoretical	147.5	17.80	22.50
K-band (22.25 GHz)	Measured	144.74	19.22	24.92
(22.23 3.12)	Difference	-2.76	1.42	2.42
K _a -band (33.25 GHz)	Theoretical	146.20	13.10	16.90
	Measured	144.74	14.11	18.02
	Difference	-1.46	1.01	1.12

^{*}The theoretical focal distance is the focal length in the datasheet, while the measured focal distance is the distance of the closest XY measured plane. Source: Elaborated by the authors.

Lastly, although the higher frequency of one antenna coincides with the lower frequency of the next frequency band, it is prudent to compare both beam waists because the lens design may be different, resulting in differences in the focal length and in the E- and H-planes.

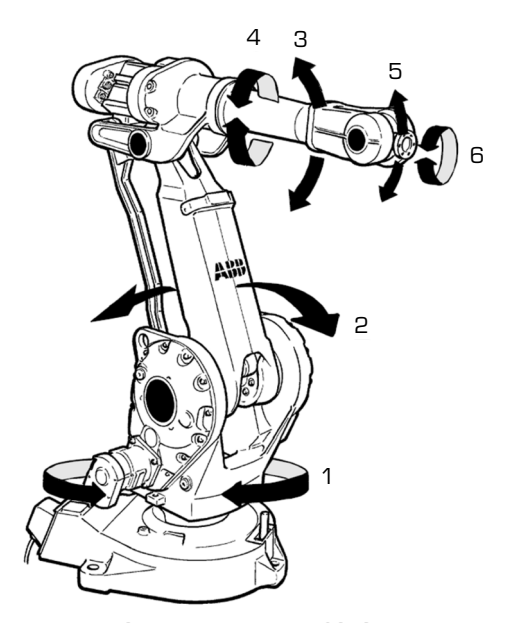
SOURCES OF ERRORS

The first source of error may arise from the wrong choice of the number of points in the scanning mesh. Equation 2 certifies that each step is at least half of the minimum wavelength, respecting the Nyquist rate (Landau 1967). However, great attention must be paid to insert the same steps on both RAPID and Python routines to avoid uncoupling.



The alignment of the probe and AUT may result in a decentralized peak of power, since the Python routine normalizes the VNA at the center position inserted in the RAPID routine. Some antennas may not have the highest power at the measured center position due to misalignment of the antenna components, and the easiest way to deal with it would be to find the highest power to normalize the VNA manually and perform a scan without automatic normalization. Another alternative would be a post-processing normalization, which is a better option when working with multiple planes because the main lobe of the AUT may not be parallel to the NF probe. This is also better when scanning multiple planes of antennas with lenses, since the first plane may be a low power region, especially if the distance between the NF probe and AUT is much smaller than the focal length.

While measuring a large planar area, the robotic arm axes may reach their limit and return an out-of-range error. Also, after a certain height, the robotic arm rotates its axis 4 (Fig. 19) in an opposite direction to the usual one based on the central position, which limits the scan area. The easiest alternatives to overcome this issue would be to use the joint-movement (MoveJ) command instead of the linear-movement (MoveL) to traverse this point, but the MoveJ command could twist the cables and possibly break them.



Source: ABB Robotic, 2013.

Figure 19. Illustration of the robotic arm axes.

The robot precision may be a source of error (Jansen and Heberling 2025), since there is no redundant system to monitor the spatial coordinates. However, all measurements presented here have consistent results with the lenses' datasheets, with a maximum beam waist error of 3.17 mm that could probably be reduced by changing the XY scan distance and increasing the scan resolution.

Mechanical issues with the robotic arm may be a source of error as well. The center position must be acquired with the FlexPendant, where the values of XYZ position and orientation must be manually inserted into the RAPID and Python routines. However, old and worn-out brakes may cause a difference in position when operating the robotic arm with the FlexPendant and when the RAPID routine is running. This is especially problematic if the orientation values change when switching from automatic to manual operation, because the NF probe may be fine aligned by rotating each axis individually with the FlexPendant.

LIMITATIONS

This system is limited to raster planar scans only. Starburst scanning may be possible to implement with a more complex "for loop" in the RAPID script. Cylindrical and spherical evaluation may also be possible by changing linear movements to circular movements (MoveC command) in the RAPID script. However, the scanning area would be considerably smaller.



CONCLUSION

It was demonstrated here that an outdated robotic arm can be used to perform planar raster NF measurements of different microwave horn antennas with lenses. Measurements were performed with X-, K_u , K-, and K_a -band lenses. Several planes were automatically scanned, saving operation time. The measured beam waists are consistent with the datasheets, with a theoretical and measured difference between 0.24 and 3.17 mm. By using an outdated robotic arm, the system costs are reduced, but the complexity increases. Also, the robotic arm is an alternative to the regular planar array NF setup measurement, since it has the advantage of saving space and performing co- and cross-polarization measurements automatically. The sources of errors and limitations were discussed here. The post-script Python source and data of all microwave horn antenna lenses are available online. Although this setup is more complex to implement and operate, using an outdated robotic arm may be a viable alternative to be implemented at laboratories with limited budgets.

CONFLICT OF INTEREST

There is no conflict of interest.

AUTHORS' CONTRIBUTION

Conceptualization: Boss AFN, Kawassaki GN; Data Curation: Boss AFN; Formal Analysis: Boss AFN; Funding Acquisition: Kawassaki GN, Rezende MC, Baldan MR; Investigation: Boss AFN, Cruz EAA, Andrade AS; Methodology: Kawassaki GN, Boss AFN; Project Administration: Kawassaki GN; Resources: Kawassaki GN, Baldan MR; Software: Boss AFN, Cruz EAA; Supervision: Baldan MR, Boss AFN; Validation: Cruz EAA, Andrade AS; Visualization: Boss AFN; Writing – Original Draft: Boss AFN; Writing – Review & Editing: Boss AFN, Rezende MC; Final approval: Boss AFN.

DATA AVAILABILITY STATEMENT

The data are available in https://github.com/afnboss/nf-lens-horn-antenna

FUNDING

Conselho Nacional de Desenvolvimento Científico e Tecnológico 🔅
Grant Nos. 314148/2025-6; 314167/2025-0; 304149/2025-2; 306836/2023-8; 405969/2022-8
Financiadora de Estudos e Projetos 🔅
Grant No: 01.22.0305.01.

ACKNOWLEDGMENTS

The authors would like to thank the company Engtelco for the robotic arm and the NF probes.

REFERENCES

ABB Robotics (2003) CAD Model, DXF/DWG, IRB 2400, 12kg-155, M2000, rev01. Västerås, Sweden: ABB Robotics. [accessed Jun 4 2025]. https://library.abb.com/d/IRB2400_10_M2000_REV1_DXFDWG_C



ABB ROBOTICS. Manual de operação – IRC5 com FlexPendant. 3HAC16590-6, 2013. [accessed Sept 26 2025]. https://docente.ifsc.edu.br/rafael.grebogi/MaterialDidatico/Mecatronica/Robotica/Material%20Robot%20ABB/pt/3HAC16590-pt.pdf

ABB Robotics (2010) Technical reference manual: RAPID instructions, functions and data types. 3HAC 16581-1. Västerås, Sweden: ABB Robotics. [accessed Jun 4 2025]. https://library.e.abb.com/public/688894b98123f87bc1257cc50044e809/Technical%20reference%20manual_RAPID_3HAC16581-1_revJ_en.pdf

ABB Robotics (2024) Product Specification S4Cplus M2000/BaseWare OS 4.0. Västerås, Sweden: ABB Robotics. [accessed Jun 4 2025]. https://library.e.abb.com/public/b0cf5a85b4b7e911c1257b4b00521469/EngS4Cplus_spec_Rev4.pdf

Anteral (May 2 2022a) LHA-F-WR90. X-Band Focusing Lens Horn Antenna. Pamplona: Anteral. [accessed Jun 4 2025]. https://anteral.com/datasheets/focusing-lens-horn-antenna-wr90.pdf

Anteral (May 2 2022b) LHA-F-WR62. Ku-Band Focusing Lens Horn Antenna. Pamplona: Anteral. [accessed Jun 4 2025]. https://anteral.com/datasheets/focusing-lens-horn-antenna-wr62.pdf

Anteral (Jan 23 2023) LHA-F-WR42. K-Band Focusing Lens Horn Antenna. Pamplona: Anteral. [accessed Jun 4 2025]. https://anteral.com/datasheets/focusing-lens-horn-antenna-wr42.pdf

Anteral (n.d.) LHA-F-WR28. Ka-Band Focusing Lens Horn Antenna. Pamplona: Anteral. [accessed Jun 4 2025]. https://anteral.com/datasheets/focusing-lens-horn-antenna-wr28.pdf

Bachynski M, Bekefi G (1956) Aberrations in circularly symmetric microwave lenses. IRE Trans Antennas Propag 4(3), 412-421. https://doi.org/10.1109/TAP.1956.1144395

Chen ZN, Li T, Xianming Q, Shi J, Li S, Su Y (2023) Microwave Metalens Antennas. Proc IEEE 111(8), 978-1010. https://doi.org/10.1109/JPROC.2023.3287599

Good B, Ransom P, Simmons S, Good A, Mirotznik MS (2012) Design of graded index flat lenses with integrated antireflective properties. Microw Opt Technol Lett 54(12), 2774-2781. https://doi.org/10.1002/mop.27198

Gordon JA, Novotny DR, Francis MH, Wittmann RC, Curtin A, Butler ML, Guerrieri JR (2015) Millimeter-wave near-field measurements using coordinated robotics. IEEE Trans Antennas Propag 63(12), 5351-5362. https://doi.org/10.1109/TAP.2015.2496110

Greegor RB, Parazzoli CG, Nielsen JA, Thompson MA, Tanielian MH, Vier DC, Schultz S, Smith DR, Schurig D (2007) Microwave focusing and beam collimation using negative index of refraction lenses. IET Microw Antennas Propag 1(1), 108-115. https://doi.org/10.1049/iet-map:20060071

 $Han\,DH,\,Wei\,XC,\,Wang\,D,\,Gao\,RXK\,(2025)\,An\,improved\,spectral\,probe\,calibration\,for\,near-field\,to\,far-field\,transformation.\\ IEEE\,Trans\,Instrum\,Meas\,74,\,1-8.\,https://doi.org/10.1109/TIM.2025.3551828$

Hisatake S (2022) Near-field measurement and far-field characterization of antennas in microwave, millimeter-wave and THz wave band based on photonics. Paper presented 2022 International Symposium on Antennas and Propagation (ISAP). IEEE; Sydney, Australia. https://doi.org/10.1109/ISAP53582.2022.9998761

Jansen H, Heberling D (2025) Numerical analysis of positioning errors in irregular near-field antenna measurements using robot-based systems. Paper presented 2025 19th European Conference on Antennas and Propagation (EuCAP). IEEE; Stockholm, Sweden. http://doi.org/10.23919/EuCAP63536.2025.11000035

Landau HJ (1967) Sampling, data transmission, and the Nyquist rate. Proc IEEE 55(10), 1701-1706. https://doi.org/10.1109/PROC.1967.5962



Lebrón RM, Salazar JL, Fulton C, Duthoit S, Schmidt D, Palmer R (2016) A novel near-field robotic scanner for surface, RF and thermal characterization of millimeter-wave active phased array antenna. Paper presented 2016 IEEE International Symposium on Phased Array Systems and Technology (PAST). IEEE; Waltham, MA, USA. https://doi.org/10.1109/ARRAY.2016.7832657

Liu Y, Wang Z, Xu J, Ouyang C, Mu X, Schober R (2023) Near-field communications: A tutorial review. IEEE Open J Commun Soc 4, 1999-2049. https://doi.org/10.1109/OJCOMS.2023.3305583

Nikitin P, Rao KVS, Lazar S (2007) An overview of near field UHF RFID. Paper presented 2007 IEEE International Conference on RFID. IEEE; Grapevine, Texas, USA. https://doi.org/10.1109/RFID.2007.346165

Novotny DR, Gordon JA, Allman MS, Guerrieri JR, Curtin AE (2017) Three antenna ranges based on articulated robotic arms at the national institute of standards and technology: Usability for over-the-air and standard near-field measurements. Paper presented 2017 IEEE Conference on Antenna Measurements & Applications (CAMA). IEEE; Tsukuba, Japan. https://doi.org/10.1109/CAMA.2017.8273367

Parini C, Gregson S, McCormick J, van Rensburg DJ (2014) Theory and practice of modern antenna range measurements. Stevenage: Institution of Engineering and Technology. https://doi.org/10.1049/PBEW055E

Petre P, Sarkar TK (1994) Planar near-field to far-field transformation using an array of dipole probes. IEEE Trans Antennas Propag 42(4), 534-537. https://doi.org/10.1109/8.286223

Roper DA, Good BL, McCauley R, Yarlagadda S, Smith J, Good A, Pa P, Mirotznik MS (2014) Additive manufacturing of graded dielectrics. Smart Mater Struct 23(4), 045029. https://doi.org/10.1088/0964-1726/23/4/045029

Shall H, Riah Z, Kadi M (2014) A 3-D near-field modeling approach for electromagnetic interference prediction. IEEE Trans Electromagn Compat 56(1), 102-112. https://doi.org/10.1109/TEMC.2013.2274576

Slater D (1991) Near-field antenna measurements. Boston: Artech House.

Tanaka Y, Ishihara K, Hisatake S (2024) Spherical near-field measurement and far-field characterization of a 300 GHz band antenna based on an electrooptic probe with compact tabletop robotic arm. Paper presented 2024 18th European Conference on Antennas and Propagation (EUCAP). IEEE; Glasgow, United Kingdom. https://doi.org/10.23919/EuCAP60739.2024.10501022

Yaghjian A (1986) An overview of near-field antenna measurements. IEEE Trans Antennas Propag 34(1), 30-45. https://doi.org/10.1109/TAP.1986.1143727

Zarghooni B, Dadgarpour A, Denidni TA (2016) Paraffin wax-based dielectric lens for metamaterial measurement in the S-band. IET Microw Antennas Propag 10(8), 891-896. https://doi.org/10.1049/iet-map.2015.0667

